Infrared probe of the charge density wave gap in ScV_6Sn_6

D. W. Kim,[1,*] Shuyuan Liu,[1,*] Chongze Wang,[1] H. W. Nam,[1] G. Pokharel,[2] Stephen D. Wilson,[2] Jun-Hyung Cho,[1,†] and S. J. Moon[1,‡]

[1]*Department of Physics, Hanyang University, Seoul 04763, Republic of Korea*

[2]*Materials Department, University of California, Santa Barbara, California 93106, USA*

(Received 2 June 2023; revised 25 September 2023; accepted 13 October 2023; published 13 November 2023)

The V-based kagome metals AV_3Sb_5 (A = K, Rb, Cs) exhibit a cascade of exotic quantum phenomena including charge density wave (CDW) order and superconductivity. Considerable effort has been made to understand the nature of the CDW phase of AV_3Sb_5, but the origin remains elusive. A new family of the V-based kagome metals RV_6Sn_6 (R = Y, Sc, or rare-earth ions) has attracted recent interest. Among RV_6Sn_6, only ScV_6Sn_6 shows a CDW order. Thus, RV_6Sn_6 can be a new platform for investigating the nature of the CDW phase of the V-based kagome metals. Here, combining infrared spectroscopy with density-functional theory (DFT) calculations, we investigate the electronic response of RV_6Sn_6 (R = Y, Sc). While the optical conductivity $\sigma_1(\omega)$ spectra of YV_6Sn_6 show no anomaly from 10 to 300 K, those of ScV_6Sn_6 exhibit drastic changes below the CDW transition temperature $T_{CDW} \approx 92$ K: the suppression of the Drude responses and the appearance of the absorption peaks at about 34 and 270 meV. A distinct multipeak structure in the energy region between 270 and 800 meV due to the interband transitions associated with the van Hove singularities (vHSs) at the M point is hardly affected by the CDW transition, implying the robustness of the vHSs at the M point against the CDW transition. Our DFT calculations demonstrate that the vHSs at the M point remain intact in the CDW phase of ScV_6Sn_6 and the CDW gaps corresponding to the absorption peak at 270 meV open most clearly on the $k_z = 1/3$ and $1/2$ planes. The calculated phonon dispersions of the pristine phase of ScV_6Sn_6 reveal that the structural instability with the imaginary phonon frequencies on the A-H-L plane ($k_z = 1/2$) and along the $\bar{M}$-$\bar{K}$ line ($k_z = 1/3$) induces the out-of-plane charge modulation, indicating that the CDW transition of ScV_6Sn_6 is associated with its structural phase transition.

DOI: 10.1103/PhysRevB.108.205118

I. INTRODUCTION

The kagome lattice is a two-dimensional network that consists of hexagons and corner-sharing triangles. By virtue of the inherent geometric character, the kagome lattice hosts unique electronic structures such as flat bands, Dirac cones, and van Hove singularities (vHSs). Consequently, the kagome lattice engenders a wide variety of novel quantum phenomena, such as nontrivial topology [1–3], spin liquid [4,5], superconductivity [6–10], spin/charge density waves, and bond orders [7,9,11].

Among the diverse physical phenomena discovered in kagome compounds, the charge density wave (CDW) phase in the V-based kagome metals AV_3Sb_5 (A = K, Rb, Cs) has drawn enormous attention due to its exotic nature. The CDW transition breaks not only time-reversal symmetry resulting in anomalous Hall effect [12,13] but also rotational symmetry potentially associated with the charge bond order [14–21]. Upon chemical doping [22–27] or applying pressure [28–30], the superconducting state emerges at the expense of the CDW order.

Due to the close connections with the superconductivity and other symmetry-broken phases, the CDW phase of AV_3Sb_5 has been studied intensively, but the origin of the CDW phase remains elusive. The nesting of the vHSs arising from the saddle points at the three distinct M points was suggested to be a main driving force for the CDW transition in AV_3Sb_5 [31,32]. On the other hand, it was also proposed that the strong electron-phonon coupling [33–38] or Jahn-Teller effect [39] could be responsible for the CDW transition.

The recent discovery of the intermetallic kagome compounds RV_6Sn_6 (R = rare-earth ions) provides an opportunity to explore intriguing quantum phases stemming from the V-based kagome lattice. Topological surface states are observed in GdV_6Sn_6 and HoV_6Sn_6 [40–42] and the interplay between nontrivial band topology and the magnetism of rare-earth ion results in the anomalous Hall effect in TbV_6Sn_6 [43,44]. Strikingly, a CDW phase was observed in ScV_6Sn_6 below $T_{CDW} \approx 92$ K [45]. The CDW transition in ScV_6Sn_6 accompanies the first-order structural phase transitions [45], as observed in AV_3Sb_5 [16,46]. However, the CDW phase of ScV_6Sn_6 shows important differences from that of AV_3Sb_5. The CDW phase of ScV_6Sn_6 exhibits a $\sqrt{3} \times \sqrt{3} \times 3$ periodic lattice distortion where the displacement of the V ions is minimal [45]. This contrasts with the 2×2 lattice distortion in the CDW phase of AV_3Sb_5 where the displacement of the V ions results in the so-called star of David or trihexagonal

*These authors contributed equally to this work.
†chojh@hanyang.ac.kr
‡soonjmoon@hanyang.ac.kr

patterns [47]. We note that the 2×2 lattice distortion in the kagome lattice is expected to occur when the nesting between the van Hove singularities at the three inequivalent M points is dominant [7,9,10]. In addition, unlike AV_3Sb_5, which shows the competition between CDW and superconductivity under charge-carrier doping or applied pressure, ScV_6Sn_6 does not display an intertwined CDW and superconducting states: the CDW phase of ScV_6Sn_6 is suppressed with increasing pressure, but superconductivity does not appear up to 11 GPa [48]. These unique electronic properties of ScV_6Sn_6 provide a route to gain insights into the nature of the CDW order of the V-based kagome metals.

In order to understand the origin of the CDW phase, it is imperative to identify the CDW gap in the electronic density of states. While several spectroscopy studies on ScV_6Sn_6 have been reported, it remains inconclusive if the gap opens in the CDW phase. An infrared spectroscopy study on ScV_6Sn_6 suggested that the CDW transition induced sudden changes in the band structure without a clear signature of the formation of the CDW gap [49]. In an angle-resolved photoemission spectroscopy (ARPES) measurement, the CDW gap opening was not observed, which was attributed to the small gap size and finite energy and momentum resolutions [50]. On the other hand, another ARPES study reported the opening of the large CDW gap of about 260 meV [51]. A scanning tunneling spectroscopy (STS) study observed a partial gap opening of about 20 meV in the electronic density of states at the Fermi level [52]. To resolve this controversial issue on the CDW gap of ScV_6Sn_6, a careful and systematic spectroscopy study of the RV_6Sn_6 series is highly demanded.

In this paper, we investigate the electronic responses of RV_6Sn_6 (R = Y, Sc) single crystals by using infrared spectroscopy and density-functional theory (DFT) calculations. Our comparative study on RV_6Sn_6 enables us to resolve the CDW gap and the associated changes in the electronic response of ScV_6Sn_6 due to the CDW transition. As the temperature decreases, the optical conductivity $\sigma_1(\omega)$ spectra of YV_6Sn_6 show gradual changes without any anomaly. The onset of the CDW phase in ScV_6Sn_6 is manifested by the abrupt suppression of the Drude responses and the emergence of absorption peaks at about 34 and 270 meV. In the higher-energy region between 270 and 800 meV, a distinct multipeak structure, which can be assigned as the optical transitions involving the van Hove singularities at the M point, is commonly observed in the $\sigma_1(\omega)$ spectra of both compounds. Notably, the multi-peak structures do not display anomalous changes with decreasing the temperature, which implies the robustness of the vHSs at the M point in the CDW phase of ScV_6Sn_6. Indeed, our DFT calculations confirm that the vHSs at the M point remain intact in the CDW phase. Instead, the CDW gaps open on the $k_z = 1/3$ and $k_z = 1/2$ planes, corresponding to the observed absorption peak at about 270 meV. The phonon band calculations reveal that the pristine phase of ScV_6Sn_6 is unstable with the imaginary phonon modes on the A-L-H plane ($k_z = 1/2$) and along the $\bar{\mathrm{M}} - \bar{\mathrm{K}}$ line ($k_z = 1/3$). Our results demonstrate that the origin of the CDW order in ScV_6Sn_6 is not endemic to the in-plane electronic instability between the vHSs at the M point but can be associated with the structural instability along the out-of-plane direction.

II. METHODS

A. Infrared spectroscopy

Single crystals of YV_6Sn_6 and ScV_6Sn_6 were synthesized by using a flux-based method. Details of the single-crystal growth were described in Ref. [41]. We measured near-normal incidence reflectivity spectra $R(\omega)$ in the energy region between 5 meV and 1 eV utilizing a Fourier transform infrared spectrometer (Vertex 70v, Bruker). We used the Hagen-Rubens relation for the low-energy extrapolation of $R(\omega)$. *In situ* gold overcoating technique was employed to obtain accurate reflectivity data [53]. We obtain complex optical constants in the energy region between 0.74 and 5 eV by using a spectroscopic ellipsometer (M-2000, J. A. Woollam Co.). The optical conductivity was calculated from the $R(\omega)$ data through Kramers-Kronig transformation.

B. Density-functional theory calculations

We performed first-principles calculations within the DFT as implemented in the Vienna *Ab initio* Simulation Package (VASP) codes [54,55]. The potential of the core was described by the projector augmented-wave method [56]. For the exchange-correlation interaction between the valence electrons, we employed the generalized-gradient approximation functional of Perdew-Burke-Ernzerhof [57]. We used the plane-wave basis with a kinetic energy cutoff of 500 eV and performed the k-space integration using the $12 \times 12 \times 8k$ meshes per $1 \times 1 \times 1$ unit cells. All atoms were allowed to relax along the calculated forces until all the residual force components were less than 0.001 eV/Å. The phonon dispersions were calculated using the finite displacement method implemented in the PHONOPY software [58] with a $3 \times 3 \times 2$ supercell. The unfolded band structure was calculated with the VASPKIT software [59]. Optical conductivity calculations were performed in the WANNIER90 program [60] with a $40 \times 40 \times 40$ k mesh in the primitive cells of the pristine and $\sqrt{3} \times \sqrt{3} \times 3$ CDW structures.

III. RESULTS AND DISCUSSION

Raw reflectivity $R(\omega)$ spectra of YV_6Sn_6 and ScV_6Sn_6 are shown in Figs. 1(a) and 1(b), respectively. The far-infrared reflectivities of both YV_6Sn_6 and ScV_6Sn_6 increase toward zero energy, indicating metallic properties. In the higher-energy region between 270 and 800 meV, the $R(\omega)$ of YV_6Sn_6 and ScV_6Sn_6 share a common multipeak structure. A clear distinction between the far-infrared responses of the two compounds is found in the lower-energy region. As the temperature decreases, the reflectivity spectra of YV_6Sn_6 below 200 meV is enhanced gradually without any anomaly. In sharp contrast, the $R(\omega)$ spectra of ScV_6Sn_6 in the energy region between 34 and 200 meV are suppressed substantially below $T_{\mathrm{CDW}} \approx 92$ K, and those below 34 meV increase toward unity faster than those at higher temperatures. This temperature evolution of $R(\omega)$ suggests the formation of an absorption peak due to the CDW transition [61,62] of ScV_6Sn_6 [45].

The real parts of the optical conductivity spectra $\sigma_1(\omega)$ of YV_6Sn_6 and ScV_6Sn_6 are displayed in Figs. 1(c)–1(f). We note that the gross spectral features of $\sigma_1(\omega)$ of the two

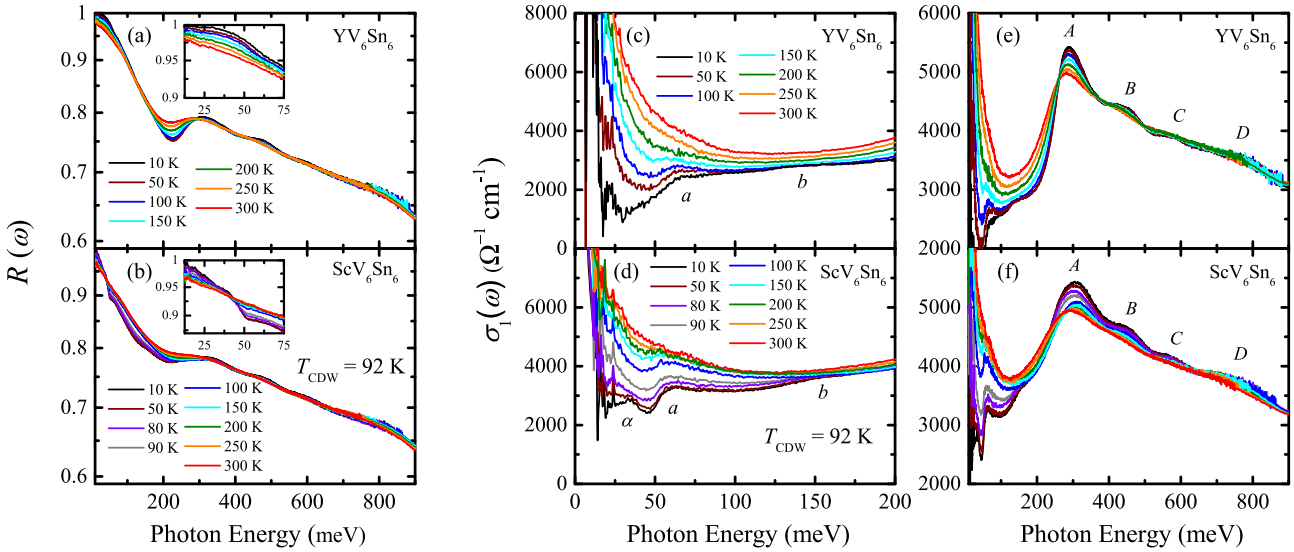

FIG. 1. Temperature-dependent reflectivity spectra $R(\omega)$ of (a) YV_6Sn_6 and (b) ScV_6Sn_6. Insets of (a) and (b) display $R(\omega)$ of YV_6Sn_6 and ScV_6Sn_6 below 75 meV, respectively. Temperature-dependent optical conductivity $\sigma_1(\omega)$ below 200 meV of (c) YV_6Sn_6 and (d) ScV_6Sn_6. Temperature-dependent optical conductivity $\sigma_1(\omega)$ below 900 meV of (e) YV_6Sn_6 and (f) ScV_6Sn_6.

compounds are similar, reflecting that they share the electronic structure of V-based kagome lattice. In the energy region between 270 and 800 meV, the $\sigma_1(\omega)$ data of both compounds show four absorption peaks, labeled as A, B, C, and D [Figs. 1(e) and 1(f)]. These peaks can be assigned as interband transitions involving the vHS in the electronic band structure, which will be discussed below. At lower energies, the Drude-like response centered at zero energy is observed. As the temperature decreases, the Drude-like peaks become narrower and two broad peaks at 60 meV (a) and 142 meV (b) are resolved. Similar low-energy peaks are detected below 500 meV in the optical response of kagome metals such as AV_3Sb_5, RMn_6Sn_6, and Fe_3Sn_2 which shift to lower energies upon cooling [36,37,63–65]. The low-energy peaks of such kagome metal compounds are attributed to a so-called localization peak or a displaced Drude peak, suggesting that they result from many-body effects that hinder charge transport. The peaks a and b of YV_6Sn_6 and ScV_6Sn_6 exhibit a slight blueshift with decreasing the temperature, indicating that they could be ascribed to interband transitions. The temperature evolutions of the infrared-active phonon modes of YV_6Sn_6 and ScV_6Sn_6 are discussed in the Supplemental Material [66].

The manifestations of the onset of the CDW phase in ScV_6Sn_6 can be seen from the clear distinctions between the $\sigma_1(\omega)$ spectra of the two compounds. Upon entering the CDW phase below $T_{CDW} \approx 92$K, a peak at about 34 meV, labeled as α, emerges only in $\sigma_1(\omega)$ of ScV_6Sn_6 [Figs. 1(c) and 1(d)]. The resonance energy of the peak at 34 meV coincides with the energy position of the kink in $R(\omega)$ below T_{CDW} [Fig. 1(b)]. Another spectral manifestation of the CDW transition can be found in the energy region where the peak A is located. As the temperature decreases from 300 to 100 K, the peak A shows a gradual narrowing and a slight blueshift. However, upon cooling across $T_{CDW} \approx 92$ K, the peak A appears to be enhanced abruptly and to shift to lower energies [Fig. 1(f)]. This contrasts with the continuous narrowing and blueshift of the peak A in $\sigma_1(\omega)$ of YV_6Sn_6 without any anomalies with decreasing the temperature [Fig. 1(e)].

In order to gain quantitative information on the temperature evolution of the electronic response, we analyze the $\sigma_1(\omega)$ by using Drude-Lorentz oscillator model:

$$\sigma_1(\omega) = \sum_k \frac{\omega_{p,k}^2}{4\pi} \frac{\gamma_{D,k}}{\omega^2 + \gamma_{D,k}^2} + \sum_j \frac{S_j^2}{4\pi} \frac{\omega^2 \gamma_j}{\left(\omega^2 - \omega_{0,j}^2\right)^2 + \omega^2 \gamma_j}. \quad (1)$$

Here, $\omega_{p,k}$ and $\gamma_{D,k}$ correspond to the plasma frequency and the scattering rate of the Drude oscillator, respectively. S_j, γ_j, and $\omega_{0,j}$ are the strength, the width, and the resonant frequency of the Lorentz oscillator, respectively. The representative results of the Drude-Lorentz oscillator model fit of $\sigma_1(\omega)$ of YV_6Sn_6 and ScV_6Sn_6 are shown for the 10 and 300 K data in Figs. 2(a)–2(d). Two Drude oscillators with different scattering rates are required to fit the $\sigma_1(\omega)$. We label the narrow Drude peak as D1 and the broad one as D2. Six Lorentz oscillators are used to fit the interband transitions: the peaks a, b, A, B, C, and D. For ScV_6Sn_6, an additional Lorentz oscillator is needed to reproduce the distinct absorption peak α at about 34 meV. The optical conductivity data at the other measurement temperatures are fitted using the same protocol.

The temperature evolutions of the optical excitations extracted from the Drude-Lorentz oscillator model fit are summarized in Figs. 2(e)–2(j). The Drude responses and the peak A of YV_6Sn_6 show monotonous temperature dependence. The spectral weight (SW) of the narrow Drude peak (D1) is almost temperature independent [Fig. 2(e)], whereas that of the broad Drude peak (D2) is slightly suppressed as the temperature decreases [Fig. 2(f)]. The scattering rates of both Drude peaks are reduced gradually with decreasing the temperature [Figs. 2(e) and 2(f)]. The SW of the peak A of

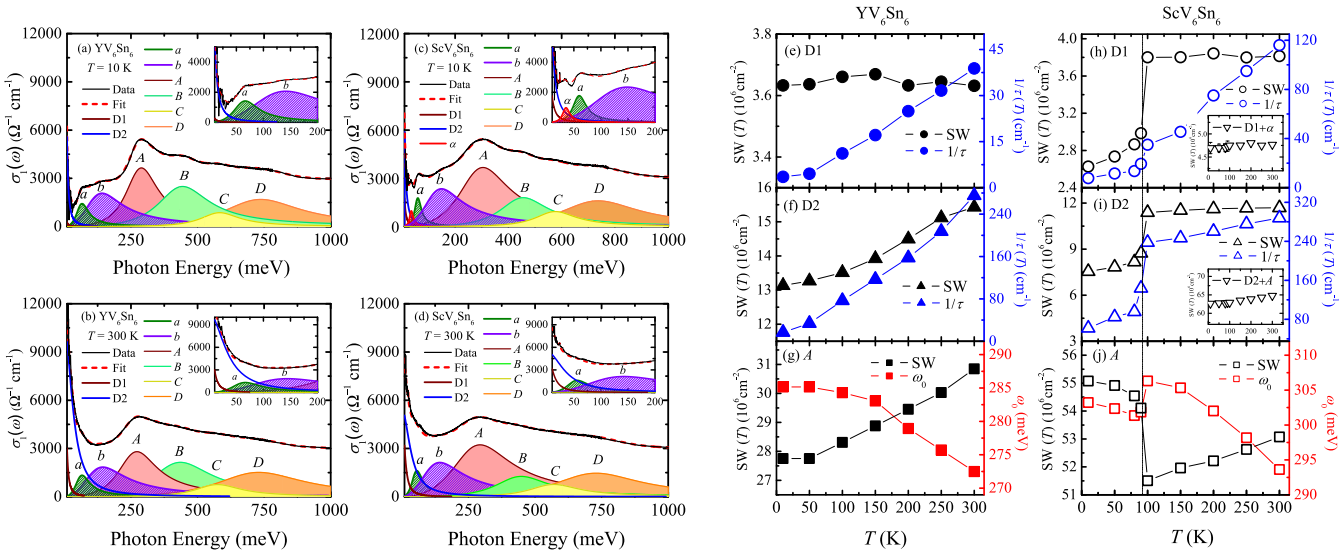

FIG. 2. Drude-Lorentz oscillator model analyses on $\sigma_1(\omega)$ of (a), (b) YV_6Sn_6 and (c), (d) ScV_6Sn_6 at 10 and 300 K, respectively. Solid lines centered at zero energy represent two Drude peaks, D1 and D2. Seven Lorentz oscillators are used to reproduce optical excitations at higher energies, i.e., peaks α, a, b, A, B, C, and D. Insets show fitting results below 200 meV. Temperature-dependent SWs and widths of the peaks D1, D2, and A for YV_6Sn_6 (e), (f), (g) and ScV_6Sn_6 (h), (i), (g). Insets of (h) and (i) show sum of the SWs of peaks D1 and α and SWs of peaks D2 and A, respectively. Dashed lines in (h), (i), and (j) denote the CDW transition temperature T_{CDW} of ScV_6Sn_6.

YV_6Sn_6 decreases slightly and shifts to higher energies at lower temperatures [Fig. 2(g)].

The parameters of the Drude responses and the peak A of ScV_6Sn_6 reveal striking anomalies associated with the CDW transition at $T_{CDW} \approx 92$ K. The SWs and the scattering rates of both Drude peaks display abrupt suppressions below T_{CDW} [Figs. 2(h) and 2(i)], which is a characteristic optical response of various materials with density wave ground states including Fe-based superconductors [61,69] and AV_3Sb_5 [31,36,37,63]. In addition to these changes in the low-energy response, the abrupt increase in the SW and the redshift of the resonance energy of the peak A upon entering the CDW phase are registered [Fig. 2(j)]. The latter observation suggests the appearance of an optical excitation due to the CDW transition of which resonance energy is a little bit lower than that of the peak A.

The difference optical conductivity spectra shown in Figs. 3(a), 3(b), and 3(e) enable us to identify the formation of the CDW gap and its magnitude. The difference spectra $\sigma_1(\omega, T) - \sigma_1(\omega, 300\,\mathrm{K})$ in Figs. 3(a) and 3(b) demonstrate the emergence of the optical excitation at about 270 meV in the CDW phase of ScV_6Sn_6. We estimate the magnitude of the CDW gap ($2\Delta_{CDW}$) via the maximum of the spectral weight transfer (orange arrow) and the zero crossing (red arrow) of the difference spectra $\sigma_1(T) - \sigma_1(100\,\mathrm{K})$ in Fig. 3(e) [36]. The former (latter) method yields $2\Delta_{CDW} \approx 270$ meV (180 meV). Since the value from the maximum of the SW transfer method can represent the resonance energy of the optical excitation across the CDW gap, we adopt $2\Delta_{CDW} \approx 270$ meV for the following discussion. Figure 3(f) shows the temperature dependences of the $2\Delta_{CDW}$, which shows the deviation from the BCS-type mean-field behavior. The abrupt suppression of the $2\Delta_{CDW}$ near T_{CDW} indicates the first-order character of the CDW transition of ScV_6Sn_6 [49], which is reminiscent of AV_3Sb_5 [36,37,63] and FeGe [70].

A close inspection of the SWs of the Drude peaks and the optical excitations at about 34 and 270 meV which emerge below T_{CDW} reveals intriguing correlations. We find that the amount of the decrease in the SW of the narrow Drude peak (D1) is very similar to the SW of the lower-energy optical excitation (α) at about 34 meV. The sum of the SWs of the peak D1 and the 34-meV peak below T_{CDW} are almost conserved, as shown in the inset of Fig. 2(h). In addition, the magnitude of the decrease in the SW of the broad Drude peak (D2) below T_{CDW} is almost the same as that of the increase in the SW of the peak A below T_{CDW}, resulting in the conservation of the sum of the SWs of the peak A and the D2 [the inset of Fig. 2(i)].

The sum-rule analysis also suggests that the excitation at about 270 meV in $\sigma_1(\omega)$ of ScV_6Sn_6 results from the opening of the CDW gap. The opening of a density wave gap triggers the suppression of the Drude peak and the shift of the SW into an optical excitation across the density wave gap at higher energies. The optical SWs obtained by integrating $\sigma_1(\omega)$, $\mathrm{SW}(\omega) = \int_0^{\omega} \sigma_1(\omega')d\omega'$ are shown in Figs. 3(c) and 3(d). The temperature evolution of $\sigma_1(\omega)$ of YV_6Sn_6 is mostly driven by the narrowing of the two Drude peaks with decreasing the temperature [Fig. 1(c)]. The corresponding behavior in the $\mathrm{SW}(\omega)$ is a monotonous increase with lowering the temperature in the energy region below 150 meV at which the sum rule is satisfied [Fig. 3(c)]. For ScV_6Sn_6, while the $\mathrm{SW}(\omega)$ at the energies below about 30 meV increases with decreasing the temperature, that in the energy region between 30 and 300 meV decreases [Fig. 3(d)], indicating the suppression of the Drude peaks due to the opening of the CDW gap. The $\mathrm{SW}(\omega)$ at different temperatures merges at about 300 meV, which suggests that the SW lost by the Drude peaks piles up at energies close to about 300 meV.

Having established the manifestations of the CDW transitions in the optical response, we discuss possible origins

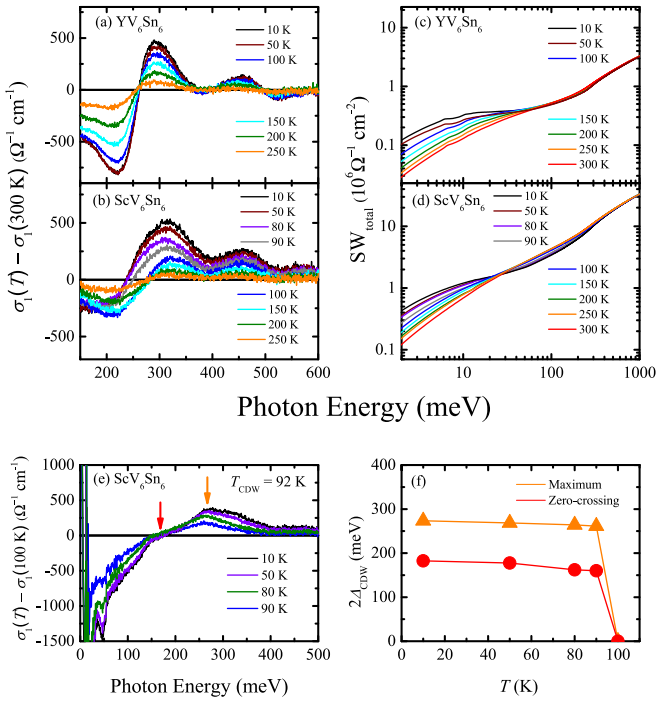

FIG. 3. Difference $\sigma_1(\omega)$ spectra $\sigma_1(T) - \sigma_1(300\,\mathrm{K})$ of (a) YV_6Sn_6 and (b) ScV_6Sn_6. Optical spectral weights (SWs) of (c) YV_6Sn_6 and (d) ScV_6Sn_6. (e) Difference $\sigma_1(\omega)$ spectra $\sigma_1(T) - \sigma_1(100\,\mathrm{K})$ of ScV_6Sn_6. Red and orange arrows indicate zero crossing and maximum of $\sigma_1(T) - \sigma_1(100\,\mathrm{K})$ spectra, respectively. (f) Temperature dependence of CDW gap ($2\Delta_{\mathrm{CDW}}$) obtained from zero crossing (red circles) and maximum of transferred peak (orange triangles).

of the CDW transition in ScV_6Sn_6. The nesting of the vHSs arising from saddle points at the M point has been regarded as one of the main origins of the CDW transition of AV_3Sb_5 [71,72]. Our DFT calculations show that the nesting of the saddle points is unlikely to drive the CDW formation in RV_6Sn_6. As shown in Figs. 4(c) and 4(d), the vHSs at the M point of YV_6Sn_6 are very close to the Fermi level [41], in contrast to ScV_6Sn_6 where the corresponding vHSs are away from the Fermi level [52,73]. Nevertheless, the CDW phase is only stabilized in ScV_6Sn_6. These results indicate that the simple nesting effect between the van Hove saddle points is not responsible for the CDW order in RV_6Sn_6. We note that similar conclusion was drawn from the ARPES study of Cs surface-doped $CsTi_3Bi_5$ [74].

The temperature evolution of the high-energy interband transitions (the peaks A, B, C, and D) in conjunction with the results from the DFT calculations supports the robustness of the vHSs at the M point with the CDW transition of ScV_6Sn_6. At the temperatures above T_{CDW}, the resonance energies of the peaks A (300 meV), B (450 meV), C (570 meV), and D (760 meV) are almost the same in YV_6Sn_6 and ScV_6Sn_6 [Figs. 4(a) and 4(b)], indicating that these peaks are related to the V $3d$ orbitals [41,42,75]. The widths of the peaks A, B, C, and D are estimated to be about 140, 223, 173, and 360 meV at 10 K, respectively, which are much smaller than the typical values of the width (1∼2 eV) of the interband transitions of $3d$ transition-metal compounds [76–80], suggesting that the bands with the vHSs may be responsible for the four peaks in $\sigma_1(\omega)$ of ScV_6Sn_6. The analogous distinct multipeak structures were also observed in AV_3Sb_5 and Fe_3Sn_2 and were linked to optical transitions involving the vHSs of the flat bands/saddle points with the divergent density of states [31,37,63,64].

Our DFT calculations show that the interband transitions are related to the bands with the vHSs of the saddle points or flat bands. Figures 4(c) and 4(d) show the calculated band dispersions of YV_6Sn_6 and ScV_6Sn_6, respectively. Here, the arrows represent the interband transitions associated with the vHSs of the saddle points or the flat bands corresponding to the four peaks (A, B, C, and D) in $\sigma_1(\omega)$. For a direct comparison with the experimental data, we calculated the interband optical conductivity spectra $\sigma_{xx}(\omega)$ of ScV_6Sn_6. The calculated $\sigma_{xx}(\omega)$ in Fig. 4(e) is found to agree quite well with the experimental interband optical-conductivity data $\sigma_{1,\mathrm{interband}}(\omega)$ in Fig. 4(f) which were obtained by subtracting the Drude responses from the raw experimental optical conductivity. The theoretical $\sigma_{xx}(\omega)$ of the pristine phase displays four peaks labeled as A' (360 meV), B' (510 meV), C' (640 meV), and D'' (840 meV) of which energies are very similar to those of the peaks A, B, C, and D in $\sigma_{1,\mathrm{interband}}(\omega)$. The agreements between the experimental and theoretical conductivity data demonstrate the validity of our assignments of the interband transitions.

Possible variations of the high-energy interband transitions with temperature can signify the changes in the vHSs at the M point for RV_6Sn_6. Strikingly, the resonance energies of the peaks B, C, and D of both compounds show little change with temperature [Figs. 4(a) and 4(b)]. The robustness of these peaks can also be seen in the theoretical $\sigma_{xx}(\omega)$ in the CDW phase [Fig. 4(e)]. The resonance energies and the intensities of the interband transitions (peaks B', C', D') in the theoretical $\sigma_{xx}(\omega)$ show negligible changes due to the CDW transition.

The peak A in the experimental $\sigma_1(\omega)$ data of ScV_6Sn_6 appears to show a sudden redshift below T_{CDW}, while that of YV_6Sn_6 shows a gradual and small blueshift with decreasing the temperature. If this redshift were due to the gap opening at the saddle points, the corresponding peak should shift to higher energies. Optical spectroscopy studies of AV_3Sb_5 have shown that the opening of the partial gap at the saddle points resulted in the blueshift of the interband transition [31,37,63]. The redshift of the peak A of ScV_6Sn_6 is due to the appearance of the optical excitation across the CDW gap at the energy (∼270 meV) lower than the resonance of energy of the peak A, as implied by the analyses on the difference optical-conductivity spectra and the sum rule. The theoretical $\sigma_{xx}(\omega)$ also shows the emergence of an optical excitation (peak a') at the energy (310 meV) lower than that of the peak A' as shown in Fig. 4(e). Therefore, the temperature evolution of the high-energy interband transitions indicates that the vHSs near the M point remain robust against the CDW transition and the nesting effects do not play an important role in ScV_6Sn_6.

For kagome lattices, it appears that not only the nesting effect, but the electron-phonon coupling could be important for the CDW transition. Recent studies on AV_3Sb_5 suggest that the electronic correlation or vHSs nesting effect is too weak to realize the CDW phase [34,38,39,81,82]

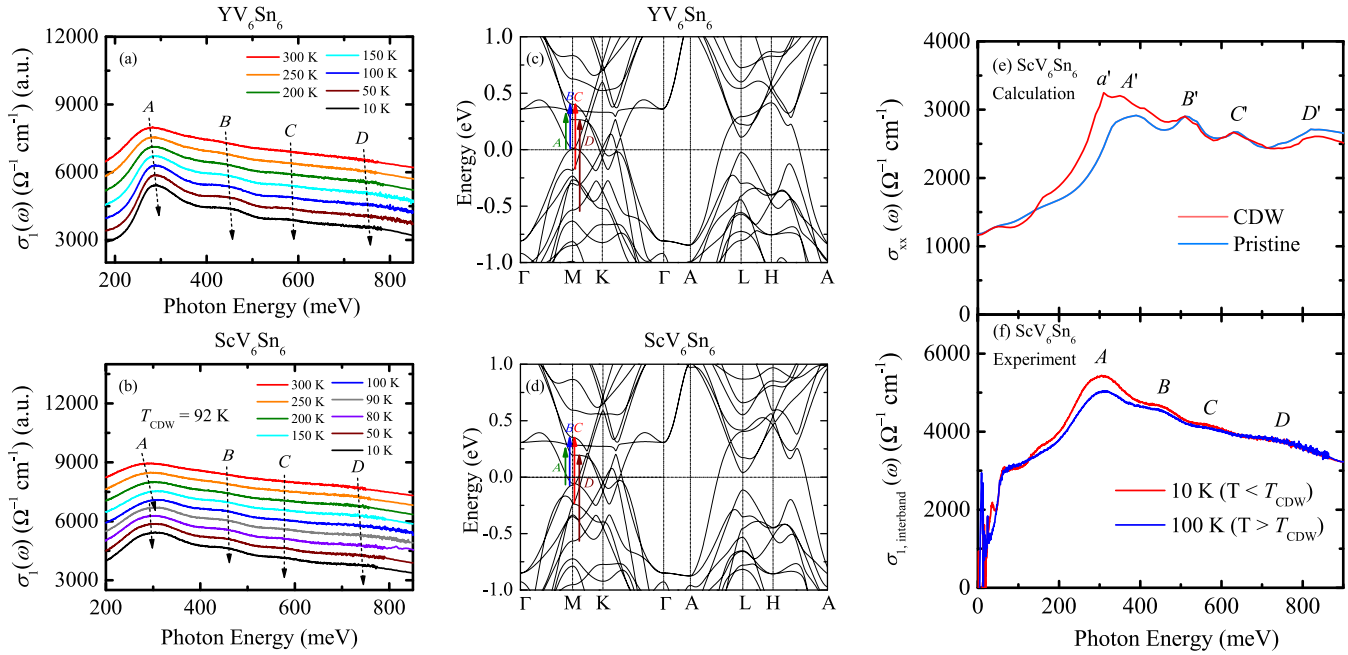

FIG. 4. $\sigma_1(\omega)$ of (a) YV_6Sn_6 and (b) ScV_6Sn_6 in energy region between 200 and 900 meV. Data are shifted vertically for clarity. Temperature dependences of resonance energies of peaks *A*, *B*, *C*, and *D* are highlighted by arrows. Electronic band structures of (c) YV_6Sn_6 and (d) ScV_6Sn_6 for pristine phase. Interband transitions corresponding to peaks *A*, *B*, *C*, and *D* are denoted by vertical arrows. (e) Calculated interband optical conductivity of ScV_6Sn_6 for pristine and CDW phases. (f) Experimental interband optical conductivity of ScV_6Sn_6 at 100 K (pristine phase) and 10 K (CDW phase).

and the electron-phonon coupling [33–38] should be taken into account. The importance of the electron-phonon coupling was also suggested in recent time-resolved optical spectroscopy of ScV_6Sn_6 [50] and inelastic x-ray- and diffuse scattering [83].

To assess the importance of the electron-phonon coupling for the CDW transition in ScV_6Sn_6, we calculate the phonon band dispersions of YV_6Sn_6 and ScV_6Sn_6. As shown in Figs. 5(a) and 5(b), the phonon band structures of the pristine phase of YV_6Sn_6 and ScV_6Sn_6 exhibit no imaginary frequencies at the *M* point where AV_3Sb_5 kagome compounds have imaginary phonon frequencies [16,24,32,84]. This result reflects the irrelevance of the Fermi surface nesting between the vHSs at the *M* point for the CDW phase of ScV_6Sn_6. Instead, we find that the multiple imaginary phonon modes exist on the *A*-*L*-*H* ($k_z = 1/2$) plane and along the $\bar{\mathrm{M}} - \bar{\mathrm{K}}$ line ($k_z = 1/3$), which can lead to the $\sqrt{3} \times \sqrt{3} \times 2$ and $\sqrt{3} \times \sqrt{3} \times 3$ lattice distortions, respectively.

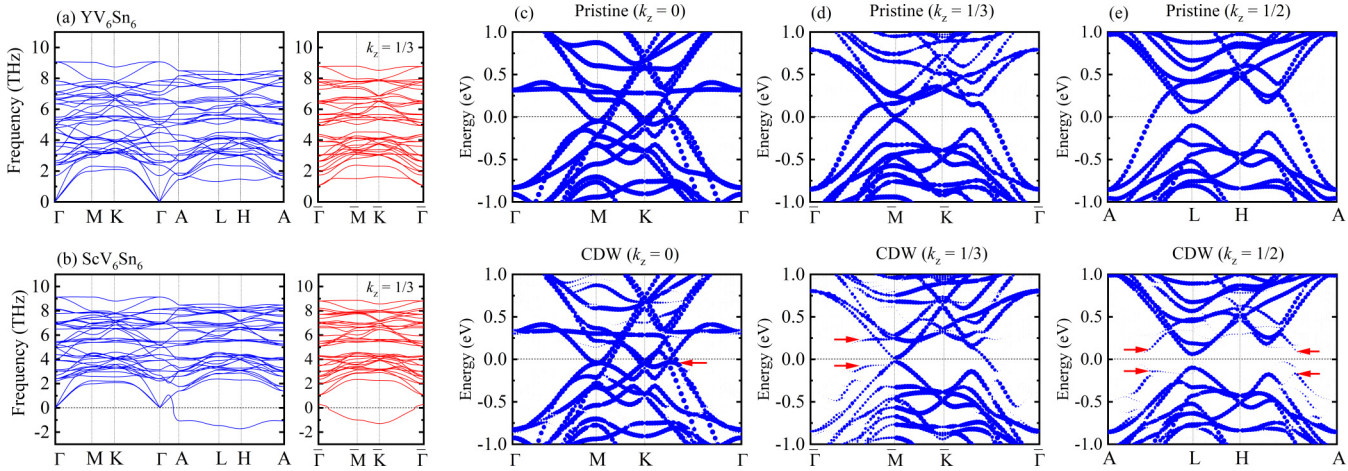

FIG. 5. Calculated phonon dispersions of (a) YV_6Sn_6 and (b) ScV_6Sn_6 for the pristine phase along the $\Gamma - M - K$ ($k_z = 0$), *A*-*H*-*L* ($k_z = 1/2$) (left panel), and $\bar{\Gamma}$-$\bar{\mathrm{M}}$-$\bar{\mathrm{K}}$ paths ($k_z = 1/3$) (right panel). Unfolded electronic band structures of ScV_6Sn_6 in pristine and $\sqrt{3} \times \sqrt{3} \times 3$ CDW phases for (c) $k_z = 0$, (d) $k_z = 1/3$, and (e) $k_z = 1/2$. Band shift on $k_z = 0$ plane and CDW gap openings on $k_z = 1/3$ and $k_z = 1/2$ planes are indicated by red arrows in (c), (d), and (e), respectively.

In order to examine how the electronic structure of ScV_6Sn_6 changes under the lattice distortion, we calculate the electronic band structure of the CDW phase of ScV_6Sn_6. We adopt the $\sqrt{3} \times \sqrt{3} \times 3$ CDW phase which was identified by the x-ray- and neutron-diffraction measurements [45]. Figures 5(c)–5(e) show the unfolded electronic band structure of the pristine and CDW phases of ScV_6Sn_6. We find that the vHSs at the *M* point are unaffected by the CDW formation [Fig. 5(c)]. Instead, the CDW-induced gap openings are clearly seen along the $\bar{\Gamma}$-$\bar{M}$ line at $k_z = 1/3$ and the *A*-*L*/*H*-*A* lines at $k_z = 1/2$ [see the red arrows in Figs. 5(d) and 5(e)]. The size of the CDW gaps reaches about 270, 290, and 300 meV along the *H*-*A*, *A*-*L*, and $\bar{\Gamma}$-$\bar{M}$ lines, respectively, in good agreement with the value (270 meV) extracted from the experimental $\sigma_1(\omega)$ data. Our calculations on the phonon dispersions and the electronic band structures therefore indicate that the structural phase transition plays a crucial role in the CDW transition of ScV_6Sn_6.

The DFT calculations reveal a small downward shift of the band along the *K*-Γ line on the $k_z = 0$ plane away from the Fermi level in the CDW phase, as indicated by the red arrow in Fig. 5(c). This band shift can induce a suppression of the density of states near the Fermi level, leading to a low-energy interband transition of about 41 meV. This result is in line with our experimental observations, i.e., the suppression of the Drude response and the appearance of the absorption peak at 34 meV in $\sigma_1(\omega)$. These changes in our optical data may be relevant to the partial gap formation with the size of about 20 meV observed in a recent STS measurement of ScV_6Sn_6 [52]. Further studies are required to understand the origin of the absorption peak at 34 meV.

As a final note, we discuss the relationship among the electronic interactions of the vHSs at the *M* point, symmetry breaking, and superconductivity. Theoretical studies on kagome lattices predicted the charge bond order due to the electronic interaction between vHSs, which can induce a rotational symmetry breaking such as electronic nematicity [9,18,20]. The nematicity is closely linked to the unconventional superconductivity in the cuprate and the Fe-based superconductors [85–87]. The importance of nematicity was also suggested in recent ARPES studies of Ti-based kagome metals [88,89]. Our results show the lack of electronic interactions between the vHSs at the *M* point in ScV_6Sn_6. It should be noted that ScV_6Sn_6 shows neither a reduction to twofold rotational symmetry [52] nor the superconductivity [48], suggesting that the interdependence of the electronic interactions of the vHSs, the nematicity, and the superconductivity may hold true for the RV_6Sn_6 system.

IV. CONCLUSION

We studied the electronic responses of RV_6Sn_6 (R = Y, Sc) using infrared spectroscopy and DFT calculations, and elaborated the effects of the CDW order on the electronic structure. The distinct temperature evolutions of the optical conductivity $\sigma_1(\omega)$ of the two compounds reveal clear spectroscopic manifestations of the CDW transition. While the optical response of YV_6Sn_6 changes gradually with lowering the temperature, that of ScV_6Sn_6 shows anomalies at $T_{CDW} \approx 92$ K. Upon entering the CDW state, the Drude-like response is suppressed and the SW is shifted to higher energies for ScV_6Sn_6, resulting in the appearance of the absorption peaks at about 34 and 270 meV. The temperature evolution of the high-energy interband transitions together with DFT calculations indicates that the vHSs at the *M* point remains intact in the CDW phase and that the CDW-induced gap opens on the $k_z = 1/3$ and $k_z = 1/2$ planes, which agrees well with the absorption peaks at about 270 meV in $\sigma_1(\omega)$. The calculated phonon dispersion of the pristine phase of ScV_6Sn_6 demonstrates that the imaginary phonon modes are absent at the *M* point but are present on the *A*-*H*-*L* plane at $k_z = 1/2$ and along the $\bar{M}$-$\bar{K}$ line at $k_z = 1/3$, indicating that the structural instability along the out-of-plane direction leads to the CDW formation.

ACKNOWLEDGMENTS

This research was supported by the National Research Foundation grant of Korea (NRF) funded by the Korean government (MSIT) (Grants No. 2022R1F1A1072865, No. 2022R1A2C1005456, and No. RS-2022–00143178), Brain-Link program funded by the Ministry of Science and ICT through the National Research Foundation of Korea (Grant No. 2022H1D3A3A01077468), and Quantum Simulator Development Project for Materials Innovation through the National Research Foundation of Korea (NRF) funded by the Korean government (Ministry of Science and ICT(MSIT)) (Grant No. NRF-2023M3K5A1094813). S.D.W. and G.P. acknowledge support via the UC Santa Barbara NSF Quantum Foundry funded via the Q-AMASE-i program under award DMR-1906325. Part of this study has been performed using facilities at the IBS Center for Correlated Electron Systems, Seoul National University.

[1] A. Bolens and N. Nagaosa, Topological states on the breathing kagome lattice, Phys. Rev. B **99**, 165141 (2019).

[2] K. Sun, Z. Gu, H. Katsura, and S. Das Sarma, Nearly flatbands with nontrivial topology, Phys. Rev. Lett. **106**, 236803 (2011).

[3] M. Kang, S. Fang, L. Ye, H. C. Po, J. Denlinger, C. Jozwiak, A. Bostwick, E. Rotenberg, E. Kaxiras, J. G. Checkelsky, and R. Comin, Topological flat bands in frustrated kagome lattice CoSn, Nat. Commun. **11**, 4004 (2020).

[4] L. Balents, Spin liquids in frustrated magnets, Nature (London) **464**, 199 (2010).

[5] S. Yan, D. A. Huse, and S. R. White, Spin-liquid ground state of the S = 1/2 kagome Heisenberg antiferromagnet, Science **332**, 1173 (2011).

[6] W.-H. Ko, P. A. Lee, and X.-G. Wen, Doped kagome system as exotic superconductor, Phys. Rev. B **79**, 214502 (2009).

[7] W.-S. Wang, Z.-Z. Li, Y.-Y. Xiang, and Q.-H. Wang, Competing electronic orders on kagome lattices at van Hove filling, Phys. Rev. B **87**, 115135 (2013).

[8] M. L. Kiesel and R. Thomale, Sublattice interference in the kagome Hubbard model, Phys. Rev. B **86**, 121105(R) (2012).

[9] M. L. Kiesel, C. Platt, and R. Thomale, Unconventional Fermi surface instabilities in the kagome Hubbard model, Phys. Rev. Lett. **110**, 126405 (2013).

[10] S.-L. Yu and J.-X. Li, Chiral superconducting phase and chiral spin-density-wave phase in a Hubbard model on the kagome lattice, Phys. Rev. B **85**, 144402 (2012).

[11] H.-M. Guo and M. Franz, Topological insulator on the kagome lattice, Phys. Rev. B **80**, 113102 (2009).

[12] F. Yu, T. Wu, Z. Wang, B. Lei, W. Zhuo, J. Ying, and X. Chen, Concurrence of anomalous Hall effect and charge density wave in a superconducting topological kagome metal, Phys. Rev. B **104**, L041103 (2021).

[13] S. Y. Yang, Y. Wang, B. R. Ortiz, D. Liu, J. Gayles, E. Derunova, R. Gonzalez-Hernandez, L. Smejkal, Y. Chen, S. S. P. Parkin, S. D. Wilson, E. S. Toberer, T. McQueen, and M. N. Ali, Giant, unconventional anomalous Hall effect in the metallic frustrated magnet candidate, KV_3Sb_5, Sci. Adv. **6**, eabb6003 (2020).

[14] H. Zhao, H. Li, B. R. Ortiz, S. M. L. Teicher, T. Park, M. Ye, Z. Wang, L. Balents, S. D. Wilson, and I. Zeljkovic, Cascade of correlated electron states in the kagome superconductor CsV_3Sb_5, Nature (London) **599**, 216 (2021).

[15] H. Li, H. Zhao, B. R. Ortiz, T. Park, M. Ye, L. Balents, Z. Wang, S. D. Wilson, and I. Zeljkovic, Rotation symmetry breaking in the normal state of a kagome superconductor KV_3Sb_5, Nat. Phys. **18**, 265 (2022).

[16] N. Ratcliff, L. Hallett, B. R. Ortiz, S. D. Wilson, and J. W. Harter, Coherent phonon spectroscopy and interlayer modulation of charge density wave order in the kagome metal CsV_3Sb_5, Phys. Rev. Mater. **5**, L111801 (2021).

[17] Z. X. Wang, Q. Wu, Q. W. Yin, C. S. Gong, Z. J. Tu, T. Lin, Q. M. Liu, L. Y. Shi, S. J. Zhang, D. Wu, H. C. Lei, T. Dong, and N. L. Wang, Unconventional charge density wave and photoinduced lattice symmetry change in the kagome metal CsV_3Sb_5 probed by time-resolved spectroscopy, Phys. Rev. B **104**, 165110 (2021).

[18] M. M. Denner, R. Thomale, and T. Neupert, Analysis of charge order in the kagome metal AV_3Sb_5 ($A = $ K, Rb, Cs), Phys. Rev. Lett. **127**, 217601 (2021).

[19] L. Nie, K. Sun, W. Ma, D. Song, L. Zheng, Z. Liang, P. Wu, F. Yu, J. Li, M. Shan, D. Zhao, S. Li, B. Kang, Z. Wu, Y. Zhou, K. Liu, Z. Xiang, J. Ying, Z. Wang, T. Wu, and X. Chen, Charge-density-wave-driven electronic nematicity in a kagome superconductor, Nature (London) **604**, 59 (2022).

[20] X. Feng, K. Jiang, Z. Wang, and J. Hu, Chiral flux phase in the Kagome superconductor AV_3Sb_5, Sci. Bull. **66**, 1384 (2021).

[21] R. Tazai, Y. Yamakawa, and H. Kontani, Charge-loop current order and Z_3 nematicity mediated by bond-order fluctuations in kagome metal AV_3Sb_5 ($A = $ Cs, Rb, K) arXiv:2207.08068.

[22] Y. M. Oey, B. R. Ortiz, F. Kaboudvand, J. Frassineti, E. Garcia, R. Cong, S. Sanna, V. F. Mitrović, R. Seshadri, and S. D. Wilson, Fermi level tuning and double-dome superconductivity in the kagome metal $CsV_3Sb_{5-x}Sn_x$, Phys. Rev. Mater. **6**, L041801 (2022).

[23] M. Liu, T. Han, X. Hu, Y. Tu, Z. Zhang, M. Long, X. Hou, Q. Mu, and L. Shan, Evolution of superconductivity and charge density wave through Ta and Mo doping in CsV_3Sb_5, Phys. Rev. B **106**, L140501 (2022).

[24] M. Kang, S. Fang, J. Yoo, B. R. Ortiz, Y. M. Oey, J. Choi, S. H. Ryu, J. Kim, C. Jozwiak, A. Bostwick, E. Rotenberg, E. Kaxiras, J. G. Checkelsky, S. D. Wilson, J. H. Park, and R. Comin, Charge order landscape and competition with superconductivity in kagome metals, Nat. Mater. **22**, 186 (2023).

[25] Y. Li, Q. Li, X. Fan, J. Liu, Q. Feng, M. Liu, C. Wang, J.-X. Yin, J. Duan, and X. Li, Tuning the competition between superconductivity and charge order in the kagome superconductor $Cs(V_{1-x}Nb_x)_3Sb_5$, Phys. Rev. B **105**, L180507 (2022).

[26] T. Kato, Y. Li, K. Nakayama, Z. Wang, S. Souma, F. Matsui, M. Kitamura, K. Horiba, H. Kumigashira, and T. Takahashi, Fermiology and origin of T_c enhancement in a kagome superconductor $Cs(V_{1-x}Nb_x)_3Sb_5$, Phys. Rev. Lett. **129**, 206402 (2022).

[27] Y. Liu, Y. Wang, Y. Cai, Z. Hao, X.-M. Ma, L. Wang, C. Liu, J. Chen, L. Zhou, J. Wang, S. Wang, H. He, Y. Liu, S. Cui, B. Huang, J. Wang, C. Chen, and J.-W. Mei, Doping evolution of superconductivity, charge order, and band topology in hole-doped topological kagome superconductors $Cs(V_{1-x}Ti_x)_3Sb_5$, Phys. Rev. Mater. **7**, 064801 (2023).

[28] K. Y. Chen, N. N. Wang, Q. W. Yin, Y. H. Gu, K. Jiang, Z. J. Tu, C. S. Gong, Y. Uwatoko, J. P. Sun, H. C. Lei, J. P. Hu, and J. G. Cheng, Double superconducting dome and triple enhancement of Tc in the kagome superconductor CsV_3Sb_5 under high pressure, Phys. Rev. Lett. **126**, 247001 (2021).

[29] F. H. Yu, D. H. Ma, W. Z. Zhuo, S. Q. Liu, X. K. Wen, B. Lei, J. J. Ying, and X. H. Chen, Unusual competition of superconductivity and charge-density-wave state in a compressed topological kagome metal, Nat. Commun. **12**, 3645 (2021).

[30] F. Du, S. Luo, B. R. Ortiz, Y. Chen, W. Duan, D. Zhang, X. Lu, S. D. Wilson, Y. Song, and H. Yuan, Pressure-induced double superconducting domes and charge instability in the kagome metal KV_3Sb_5, Phys. Rev. B **103**, L220504 (2021).

[31] X. Zhou, Y. Li, X. Fan, J. Hao, Y. Dai, Z. Wang, Y. Yao, and H.-H. Wen, Origin of charge density wave in the kagome metal CsV_3Sb_5 as revealed by optical spectroscopy, Phys. Rev. B **104**, L041101 (2021).

[32] H. Tan, Y. Liu, Z. Wang, and B. Yan, Charge density waves and electronic properties of superconducting kagome metals, Phys. Rev. Lett. **127**, 046401 (2021).

[33] G. Liu, X. Ma, K. He, Q. Li, H. Tan, Y. Liu, J. Xu, W. Tang, K. Watanabe, T. Taniguchi, L. Gao, Y. Dai, H. H. Wen, B. Yan, and X. Xi, Observation of anomalous amplitude modes in the kagome metal CsV_3Sb_5, Nat. Commun. **13**, 3461 (2022).

[34] H. Luo, Q. Gao, H. Liu, Y. Gu, D. Wu, C. Yi, J. Jia, S. Wu, X. Luo, Y. Xu, L. Zhao, Q. Wang, H. Mao, G. Liu, Z. Zhu, Y. Shi, K. Jiang, J. Hu, Z. Xu, and X. J. Zhou, Electronic nature of charge density wave and electron-phonon coupling in kagome superconductor KV_3Sb_5, Nat. Commun. **13**, 273 (2022).

[35] Y. Xie, Y. Li, P. Bourges, A. Ivanov, Z. Ye, J.-X. Yin, M. Z. Hasan, A. Luo, Y. Yao, and Z. Wang, Electron-phonon coupling in the charge density wave state of CsV_3Sb_5, Phys. Rev. B **105**, L140501 (2022).

[36] E. Uykur, B. R. Ortiz, S. D. Wilson, M. Dressel, and A. A. Tsirlin, Optical detection of the density-wave instability in the kagome metal KV_3Sb_5, npj Quantum Mater. **7**, 16 (2022).

[37] M. Wenzel, B. Ortiz, S. Wilson, M. Dressel, A. A. Tsirlin, and E. Uykur, Optical study of RbV_3Sb_5: Multiple density-wave gaps and phonon anomalies, Phys. Rev. B **105**, 245123 (2022).

[38] J.-G. Si, W.-J. Lu, Y.-P. Sun, P.-F. Liu, and B.-T. Wang, Charge density wave and pressure-dependent superconductivity in the kagome metal CsV_3Sb_5: A first-principles study, Phys. Rev. B **105**, 024517 (2022).

[39] C. Wang, S. Liu, H. Jeon, and J.-H. Cho, Origin of charge density wave in the layered kagome metal CsV_3Sb_5, Phys. Rev. B **105**, 045135 (2022).

[40] S. Peng, Y. Han, G. Pokharel, J. Shen, Z. Li, M. Hashimoto, D. Lu, B. R. Ortiz, Y. Luo, H. Li, M. Guo, B. Wang, S. Cui, Z. Sun, Z. Qiao, S. D. Wilson, and J. He, Realizing kagome band structure in two-dimensional kagome surface states of RV_6Sn_6 (R = Gd, Ho), Phys. Rev. Lett. **127**, 266401 (2021).

[41] G. Pokharel, S. M. L. Teicher, B. R. Ortiz, P. M. Sarte, G. Wu, S. Peng, J. He, R. Seshadri, and S. D. Wilson, Electronic properties of the topological kagome metals YV_6Sn_6 and GdV_6Sn_6, Phys. Rev. B **104**, 235139 (2021).

[42] Y. Hu, X. Wu, Y. Yang, S. Gao, N. C. Plumb, A. P. Schnyder, W. Xie, J. Ma, and M. Shi, Tunable topological Dirac surface states and van Hove singularities in kagome metal GdV_6Sn_6, Sci. Adv. **8**, eadd2024 (2022).

[43] E. Rosenberg, J. M. DeStefano, Y. Guo, J. S. Oh, M. Hashimoto, D. Lu, R. J. Birgeneau, Y. Lee, L. Ke, M. Yi, and J.-H. Chu, Uniaxial ferromagnetism in the kagome metal TbV_6Sn_6, Phys. Rev. B **106**, 115139 (2022).

[44] G. Pokharel, B. Ortiz, J. Chamorro, P. Sarte, L. Kautzsch, G. Wu, J. Ruff, and S. D. Wilson, Highly anisotropic magnetism in the vanadium-based kagome metal TbV_6Sn_6, Phys. Rev. Mater. **6**, 104202 (2022).

[45] H. W. S. Arachchige, W. R. Meier, M. Marshall, T. Matsuoka, R. Xue, M. A. McGuire, R. P. Hermann, H. Cao, and D. Mandrus, Charge density wave in kagome lattice intermetallic ScV_6Sn_6, Phys. Rev. Lett. **129**, 216402 (2022).

[46] J. Luo, Z. Zhao, Y. Z. Zhou, J. Yang, A. F. Fang, H. T. Yang, H. J. Gao, R. Zhou, and G.-q. Zheng, Possible star-of-David pattern charge density wave with additional modulation in the kagome superconductor CsV_3Sb_5, npj Quantum Mater. **7**, 30 (2022).

[47] B. R. Ortiz, S. M. Teicher, L. Kautzsch, P. M. Sarte, N. Ratcliff, J. Harter, J. P. Ruff, R. Seshadri, and S. D. Wilson, Fermi surface mapping and the nature of charge-density-wave order in the kagome superconductor CsV_3Sb_5, Phys. Rev. X **11**, 041030 (2021).

[48] X. Zhang, J. Hou, W. Xia, Z. Xu, P. Yang, A. Wang, Z. Liu, J. Shen, H. Zhang, X. Dong, Y. Uwatoko, J. Sun, B. Wang, Y. Guo, and J. Cheng, Destabilization of the charge density wave and the absence of superconductivity in ScV_6Sn_6 under High Pressures up to 11 GPa, Materials **15**, 7372 (2022).

[49] T. Hu, H. Pi, S. Xu, L. Yue, Q. Wu, Q. Liu, S. Zhang, R. Li, X. Zhou, J. Yuan, D. Wu, T. Dong, H. Weng, and N. Wang, Optical spectroscopy and band structure calculations of the structural phase transition in the vanadium-based kagome metal ScV_6Sn_6, Phys. Rev. B **107**, 165119 (2023).

[50] M. Tuniz, A. Consiglio, D. Puntel, C. Bigi, S. Enzner, G. Pokharel, P. Orgiani, W. Bronsch, F. Parmigiani, and V. Polewczyk, Dynamics and resilience of the charge density wave in a bilayer kagome metal, arXiv:2302.10699.

[51] S. Lee, C. Won, J. Kim, J. Yoo, S. Park, J. Denlinger, C. Jozwiak, A. Bostwick, E. Rotenberg, and R. Comin, Nature of charge density wave in kagome metal ScV_6Sn_6, arXiv:2304.11820.

[52] S. Cheng, Z. Ren, H. Li, J. Oh, H. Tan, G. Pokharel, J. M. DeStefano, E. Rosenberg, Y. Guo, and Y. Zhang, Nanoscale visualization and spectral fingerprints of the charge order in ScV_6Sn_6 distinct from other kagome metals, arXiv:2302.12227.

[53] C. C. Homes, M. Reedyk, D. A. Cradles, and T. Timusk, Technique for measuring the reflectance of irregular, submillimeter-sized samples, Appl. Opt. **32**, 2976 (1993).

[54] G. Kresse and J. Hafner, Ab initio molecular dynamics for open-shell transition metals, Phys. Rev. B **48**, 13115 (1993).

[55] G. Kresse and J. Furthmüller, Efficiency of ab-initio total energy calculations for metals and semiconductors using a plane-wave basis set, Comput. Mater. Sci **6**, 15 (1996).

[56] P. E. Blöchl, Projector augmented-wave method, Phys. Rev. B **50**, 17953 (1994).

[57] J. P. Perdew, K. Burke, and M. Ernzerhof, Generalized gradient approximation made simple, Phys. Rev. Lett. **77**, 3865 (1996).

[58] A. Togo and I. Tanaka, First principles phonon calculations in materials science, Scr. Mater. **108**, 1 (2015).

[59] V. Wang, N. Xu, J.-C. Liu, G. Tang, and W.-T. Geng, VASPKIT: A user-friendly interface facilitating high-throughput computing and analysis using VASP code, Comput. Phys. Commun. **267**, 108033 (2021).

[60] G. Pizzi, V. Vitale, R. Arita, S. Blügel, F. Freimuth, G. Géranton, M. Gibertini, D. Gresch, C. Johnson, and T. Koretsune, Wannier90 as a community code: New features and applications, J. Phys.: Condens. Matter **32**, 165902 (2020).

[61] W. Hu, J. Dong, G. Li, Z. Li, P. Zheng, G. Chen, J. Luo, and N. Wang, Origin of the spin density wave instability in AFe_2As_2 (A = Ba, Sr) as revealed by optical spectroscopy, Phys. Rev. Lett. **101**, 257005 (2008).

[62] Y. Huang, H. P. Wang, W. D. Wang, Y. G. Shi, and N. L. Wang, Formation of the density wave energy gap in $Na_2Ti_2Sb_2O$: An optical spectroscopy study, Phys. Rev. B **87**, 100507(R) (2013).

[63] E. Uykur, B. Ortiz, O. Iakutkina, M. Wenzel, S. Wilson, M. Dressel, and A. Tsirlin, Low-energy optical properties of the nonmagnetic kagome metal CsV_3Sb_5, Phys. Rev. B **104**, 045130 (2021).

[64] A. Biswas, O. Iakutkina, Q. Wang, H. C. Lei, M. Dressel, and E. Uykur, Spin-reorientation-induced band gap in Fe_3Sn_2: Optical signatures of Weyl nodes, Phys. Rev. Lett. **125**, 076403 (2020).

[65] M. Wenzel, A. Tsirlin, O. Iakutkina, Q. Yin, H. Lei, M. Dressel, and E. Uykur, Effect of magnetism and phonons on localized carriers in the ferrimagnetic kagome metals $GdMn_6Sn_6$ and $TbMn_6Sn_6$, Phys. Rev. B **106**, L241108 (2022).

[66] See Supplemental Material at http://link.aps.org/supplemental/10.1103/PhysRevB.108.205118 for the discussion of the infrared-active phonon modes of and ScV_6Sn_6 and YV_6Sn_6, which also contains Refs. [67,68].

[67] U. Fano, Effects of configuration interaction on intensities and phase shifts, Phys. Rev. **124**, 1866 (1961).

[68] A. B. Kuzmenko, L. Benfatto, E. Cappelluti, I. Crassee, D. van der Marel, P. Blake, K. S. Novoselov, and A. K. Geim, Gate tunable infrared phonon anomalies in bilayer graphene, Phys. Rev. Lett. **103**, 116804 (2009).

[69] Y. M. Dai, A. Akrap, S. L. Bud'ko, P. C. Canfield, and C. C. Homes, Optical properties of AFe_2As_2, (A = Ca, Sr, and Ba) single crystals, Phys. Rev. B **94**, 195142 (2016).

[70] X. Teng, L. Chen, F. Ye, E. Rosenberg, Z. Liu, J.-X. Yin, Y.-X. Jiang, J. S. Oh, M. Z. Hasan, K. J. Neubauer, B. Gao, Y. Xie, M. Hashimoto, D. Lu, C. Jozwiak, A. Bostwick, E. Rotenberg, R. J. Birgeneau, J.-H. Chu, M. Yi, and P. Dai, Discovery of charge density wave in a kagome lattice antiferromagnet, Nature (London) **609**, 490 (2022).

[71] M. Kang, S. Fang, J.-K. Kim, B. R. Ortiz, S. H. Ryu, J. Kim, J. Yoo, G. Sangiovanni, D. Di Sante, and B.-G. Park, Twofold van Hove singularity and origin of charge order in topological kagome superconductor CsV_3Sb_5, Nat. Phys. **18**, 301 (2022).

[72] Z. Wang, S. Ma, Y. Zhang, H. Yang, Z. Zhao, Y. Ou, Y. Zhu, S. Ni, Z. Lu, and H. Chen, Distinctive momentum dependent charge-density-wave gap observed in CsV_3Sb_5 superconductor with topological Kagome lattice, arXiv:2104.05556.

[73] H. Tan and B. Yan, Abundant lattice instability in kagome metal ScV_6Sn_6, Phys. Rev. Lett. **130**, 266402 (2023).

[74] B. Liu, M. Q. Kuang, Y. Luo, Y. Li, C. Hu, J. Liu, Q. Xiao, X. Zheng, L. Huai, S. Peng, Z. Wei, J. Shen, B. Wang, Y. Miao, X. Sun, Z. Ou, S. Cui, Z. Sun, M. Hashimoto, D. Lu, C. Jozwiak, A. Bostwick, E. Rotenberg, L. Moreschini, A. Lanzara, Y. Wang, Y. Peng, Y. Yao, Z. Wang, and J. He, Tunable van Hove singularity without structural instability in kagome metal $CsTi_3Bi_5$, Phys. Rev. Lett. **131**, 026701 (2023).

[75] H. Ishikawa, T. Yajima, M. Kawamura, H. Mitamura, and K. Kindo, GdV_6Sn_6: A multi-carrier metal with non-magnetic $3d$-electron Kagome bands and $4f$-electron magnetism, J. Phys. Soc. Jpn. **90**, 124704 (2021).

[76] J. Jung, K. Kim, D. Eom, T. Noh, E. Choi, J. Yu, Y. Kwon, and Y. Chung, Determination of electronic band structures of $CaMnO_3$ and $LaMnO_3$ using optical-conductivity analyses, Phys. Rev. B **55**, 15489 (1997).

[77] M. M. Qazilbash, A. A. Schafgans, K. S. Burch, S. J. Yun, B. G. Chae, B. J. Kim, H. T. Kim, and D. N. Basov, Electrodynamics of the vanadium oxides VO_2 and V_2O_3, Phys. Rev. B **77**, 115121 (2008).

[78] S. Noh, G. Ahn, J. Seo, Z. Gai, H. N. Lee, W. S. Choi, and S. J. Moon, $(LaCoO_3)_n/(SrCoO_{2.5})_n$ superlattices: Tunable ferromagnetic insulator, Phys. Rev. B **100**, 064415 (2019).

[79] M. Imada, A. Fujimori, and Y. Tokura, Metal-insulator transitions, Rev. Mod. Phys. **70**, 1039 (1998).

[80] S. Y. Kim, M. C. Lee, G. Han, M. Kratochvilova, S. Yun, S. J. Moon, C. Sohn, J. G. Park, C. Kim, and T. W. Noh, Spectroscopic studies on the metal-insulator transition mechanism in correlated materials, Adv. Mater. **30**, e1704777 (2018).

[81] M. Liu, Z. Wang, and J.-J. Zhou, Weak electronic correlations in the kagome superconductor AV_3Sb_5 (A = K, Rb, Cs), Phys. Rev. B **105**, 235130 (2022).

[82] Z. Ye, A. Luo, J.-X. Yin, M. Z. Hasan, and G. Xu, Structural instability and charge modulations in the kagome superconductor AV_3Sb_5, Phys. Rev. B **105**, 245121 (2022).

[83] A. Korshunov, H. Hu, D. Subires, Y. Jiang, D. Călugăru, X. Feng, A. Rajapitamahuni, C. Yi, S. Roychowdhury, and M. Vergniory, Softening of a flat phonon mode in the kagome ScV_6Sn_6, arXiv:2304.09173.

[84] M. H. Christensen, T. Birol, B. M. Andersen, and R. M. Fernandes, Theory of the charge density wave in AV_3Sb_5 kagome metals, Phys. Rev. B **104**, 214513 (2021).

[85] A. E. Böhmer, J.-H. Chu, S. Lederer, and M. Yi, Nematicity and nematic fluctuations in iron-based superconductors, Nat. Phys. **18**, 1412 (2022).

[86] T.-M. Chuang, M. Allan, J. Lee, Y. Xie, N. Ni, S. Bud'ko, G. Boebinger, P. Canfield, and J. Davis, Nematic electronic structure in the "parent" state of the iron-based superconductor $Ca(Fe_{1-x}Co_x)_2As_2$, Science **327**, 181 (2010).

[87] J.-H. Chu, H.-H. Kuo, J. G. Analytis, and I. R. Fisher, Divergent nematic susceptibility in an iron arsenide superconductor, Science **337**, 710 (2012).

[88] Y. Hu, C. Le, Y. Zhang, Z. Zhao, J. Liu, J. Ma, N. C. Plumb, M. Radovic, H. Chen, A. P. Schnyder, X. Wu, X. Dong, J. Hu, H. Yang, H.-J. Gao, and M. Shi, Non-trivial band topology and orbital-selective electronic nematicity in a titanium-based kagome superconductor, Nat. Phys. (2023), doi:10.1038/s41567-023-02215-z.

[89] H. Li, S. Cheng, B. R. Ortiz, H. Tan, D. Werhahn, K. Zeng, D. Johrendt, B. Yan, Z. Wang, S. D. Wilson, and I. Zeljkovic, Electronic nematicity in the absence of charge density waves in a new titanium-based kagome metal, Nat. Phys. (2023), doi:10.1038/s41567-023-02176-3.